Geophysical Journal International

Geophys. J. Int. (2017) **211,** 1237–1253
doi: 10.1093/gji/ggx335
Advance Access publication 2017 August 3
GJI Rock and mineral physics, rheology

Migration mode of brine and supercritical CO_2 during steady-state relative permeability measurements at very slow fluid flow velocity

Tetsuya Kogure,* Yi Zhang, Osamu Nishizawa and Ziqiu Xue

CO_2 Storage Research Group, Research Institute of Innovative Technology for the Earth, Kizugawa, Kyoto 6190292*, Japan.*
E-mail: kogure@riko.shimane-u.ac.jp

Accepted 2017 August 2. Received 2017 July 30; in original form 2017 April 7

SUMMARY

Characteristics of two-phase flow for a brine–CO_2 system in Berea sandstone were investigated to understand flow mechanisms on the basis of 'ganglion dynamics' and 'connected-pathway flow', both recently established through studies using synchrotron-beam micro-X-ray CT (μCT). Relative permeability curves (RPCs) in the brine–CO_2 system were measured under steady-state conditions by calculating CO_2 saturation from medical X-ray CT images. Fluid flow velocity was less than 10^{-5} m s^{-1}, which represents the scenario of fluid movements near CO_2 diffusion fronts in reservoirs. The flow direction was perpendicular to sedimentary layers during the injections in the experiment. The differential pressure across the core at each steady-flow state generally decreases with increasing CO_2 content. This suggests a CO_2 flow regime transition from one where ganglion dynamics dominated to one where connected-pathway-flow dominated. Randomly distributed pathways appear in each layer, resulting in a critical CO_2 saturation (35–40 per cent) for achieving steady flow. The critical saturation value corresponds to the critical values reported in electrical resistivity in sandstones where the resistivity deviates from Archie's law. In contrast, for a flow direction parallel to sedimentary layers, steady-flow states are achieved when CO_2 percolation clusters (channels) appear at lower CO_2 saturation values (0–10 per cent). The flow perpendicular to bedding showed high CO_2 saturation (*ca*. 40 per cent) at the brine-rich endpoint of RPC. Then, a rapid increase in RPC appeared at the CO_2 saturation values 40–50 per cent. This suggests that the steady flow between inlet and outlet of sample ends is achieved through percolation pathways, and that the percolation clusters grow rapidly above critical saturation, as was indicated by the classical percolation theory. The relationship between sedimentary layers and flow direction seems to control the shapes of RPC, but the crucial factor is which type of CO_2 pathway dominates: channeled pathway or randomly distributed pathway.

Key words: Permeability and porosity; Hydrogeophysics; Image processing.

1 INTRODUCTION

Understanding of immiscible two-phase flow in porous media is a significant issue in various fields. For carbon dioxide capture and storage (CCS) projects, studies of immiscible two-phase flow are important to predict the fate of injected CO_2 in a saline aquifer. Recent studies have been conducted using X-ray CT scanners to observe migration processes of brine and CO_2 in reservoir rocks (e.g. Perrin & Benson 2010; Alemu *et al*. 2013; Zhang *et al*. 2014, 2015; Reynolds & Krevor 2015).

An important outcome of those experimental studies is to obtain the relative permeability curve (RPC) of brine and CO_2 in porous media. Relative permeability is defined as the ratio of the effective permeability of each fluid to the absolute permeability of a rock. The plot of each relative permeability against brine (or CO_2) saturation is referred to as the RPC. In CCS, RPC is used in reservoir simulations to describe movements of CO_2 for large time spans, and then the fate of injected CO_2 is predicted. A number of laboratory experiments have been conducted to obtain RPC for the brine–CO_2 flow system (e.g. Perrin & Benson 2010; Krevor *et al*. 2012; Akbarabadi & Piri 2013; Kogure *et al*. 2013; Pini & Benson 2013; Ruprecht *et al*. 2014; Reynolds & Krevor 2015).

The shape of RPC is not a unique function of fluid saturation. Other dependencies include fluid velocities, viscosity ratio between two fluids, fluid flow velocity and saturation history (Valavanides *et al*. 1998). The effect of fluid flow velocity on the shape of RPC is discussed with respect to the capillary number of the displacing fluid. The capillary number is defined as the product of viscosity and flow velocity divided by the surface tension between fluids

*Now at: Department of Geoscience, Interdisciplinary Graduate School of Science and Engineering, Shimane University, Matsue, Shimane 6908504, Japan.

(Lenormand *et al.* 1988). Measurement of RPC in the brine–CO_2 system under a low flow-rate condition is important because CO_2 flow velocity appears to be very small at the front of the CO_2 diffusion zone in reservoirs. Considering the scale of a CO_2 reservoir and typical injection rates of CO_2 (e.g. Perrin & Benson 2010), the fluid velocity must be below 10^{-5} m s^{-1}. However, RPC measurements so far have been conducted mostly at flow velocities higher than this. Krause & Benson (2015) proposed a flow-rate independent model named 'characteristic relative permeability'. They claimed that the effect of the subcore scale heterogeneity on relative permeability can be included in characteristic relative permeability.

Relative permeability is implicitly based on Darcy's law, and the basic flow-driving mechanism is the capillary-pressure gradient of CO_2 in the pore networks, like the often-quoted Brooks–Corey model (Brooks & Corey 1964). However, recent studies based on a micro-X-ray CT scanner (μCT) with a beam emitted from a synchrotron have revealed the movements and geometries of pore-filling fluids at micrometre scale (e.g. Berg *et al.* 2013, 2016; Rücker *et al.* 2015). Those studies provide a first-principle model for understanding flow characteristics of concurrent CO_2 and brine flow in porous media. The model can allow more sophisticated numerical simulations on two-fluid flow (Armstrong *et al.* 2016). The model consists of two elementary processes: ganglion dynamics and connected-pathway flow. Ganglion dynamics describes movement of non-wetting fluid in pores by coalescence or snap-off event in non-wetting ganglion, whereas connected-pathway flow describes the movement as through a large ganglion that connects high- and low-pressure regions and is regarded as percolated clusters in terms of percolation theory (Stauffer & Aharony 1994). Flow by ganglion dynamics and connected pathways, can coexist over a wide range of non-wetting phase saturation, 25–50 per cent, without accompanying a sharp transition between two flow regimes (Armstrong *et al.* 2016).

The use of μCT enables us to visualize coalescence and snap off in non-wetting ganglion in two-phase flow at micrometre scale. However, the μCT itself is not suitable to study flow mechanisms that are revealed by core-flooding experiments because sandstone generally contains millimetre-scale heterogeneity, which is comparable to the sample sizes used for μCT studies. A medical X-ray CT allows mapping CO_2 distributions and porosity distribution at rock-core scale with submillimetre resolution. A detailed analysis of the results obtained from a medical X-ray CT will help to bridge the flow mechanisms revealed by μCT and those observed in continuum scale.

Sandstones are modeled as reservoir rock for CCS, and generally contain layered heterogeneity consisting of millimetre size high- and low-porosity zones. In most of the previous studies on core-flooding experiments or RPC measurements of brine–CO_2 flow, the two fluids were injected in a direction parallel to the layers. In that case, the CO_2 ganglia preferentially migrate into the low capillary-pressure layers, resulting in formation of CO_2 flow channels in the high-porosity layers which usually contain larger pores and pore throats. Percolation clusters of CO_2 are formed in high-porosity layers, even in lower CO_2 saturation. Since an actual CO_2 reservoir can have a complicated geology, fluid migration in rocks should be evaluated for various types of heterogeneity with respect to flow direction.

We investigated the characteristics of two-phase flow for brine–CO_2 system by using a medical X-ray CT with a low flow-rate (low capillary number) injection into a Berea sandstone core by setting the flow direction perpendicular to sedimentary layers. The flow direction therefore crosses the high- and low-porosity layers. Changes in differential pressure across the core and CO_2 saturation distribution were measured for the drainage process using step-by-step changes in the volume ratio of CO_2 to brine in this study. We studied and will discuss the interplay between ganglion dynamics and connected-pathway flow, by analysing the differential pressure, voxel by voxel data on porosity and CO_2 saturation.

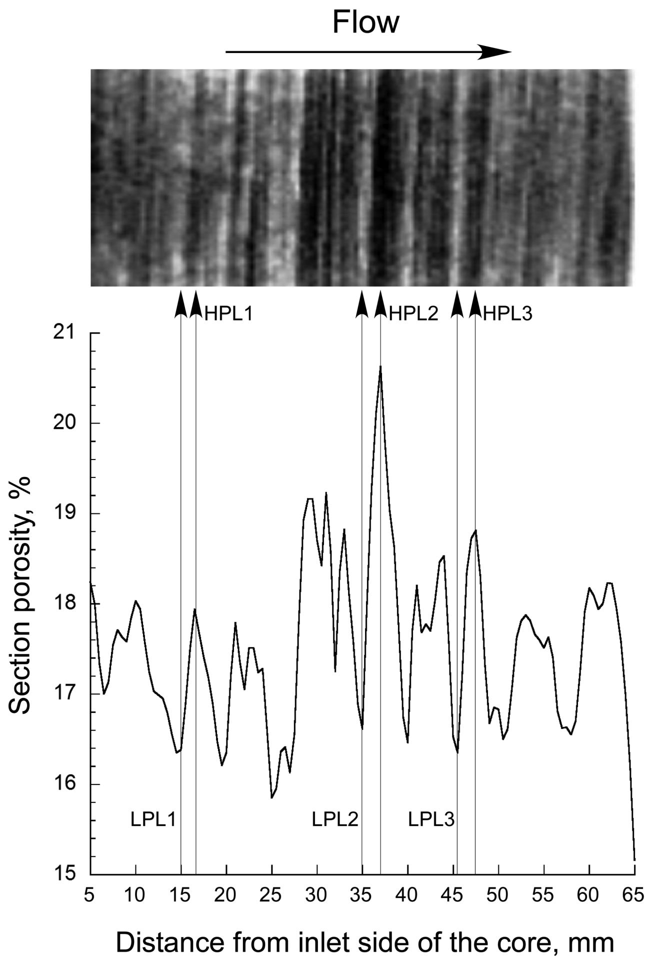

Figure 1. X-ray CT image of the Berea sandstone core used in this study and average porosity profile along the core axis. Lateral scales in the image and the graph correspond to each other. The abbreviations 'HPL' and 'LPL' indicate high- and low-porosity layers, respectively.

2 EXPERIMENTS

2.1 Specimen

The specimen was a cylindrical core of Berea sandstone with a diameter of 35 mm and a length of 70 mm (Fig. 1). The core has a layered structure with high- and low-density layers perpendicular to the core axis.

Absolute permeability, k_{abs}, measured at a confining pressure of 12 MPa and mean fluid pressure of 10 MPa prior to the relative permeability measurements was 3.1×10^{-14} m^2 (31 mD). The bulk porosity was 17.5 per cent, which corresponds to a sample pore volume of 11.8 mL. Zhang *et al.* (2014) performed mercury

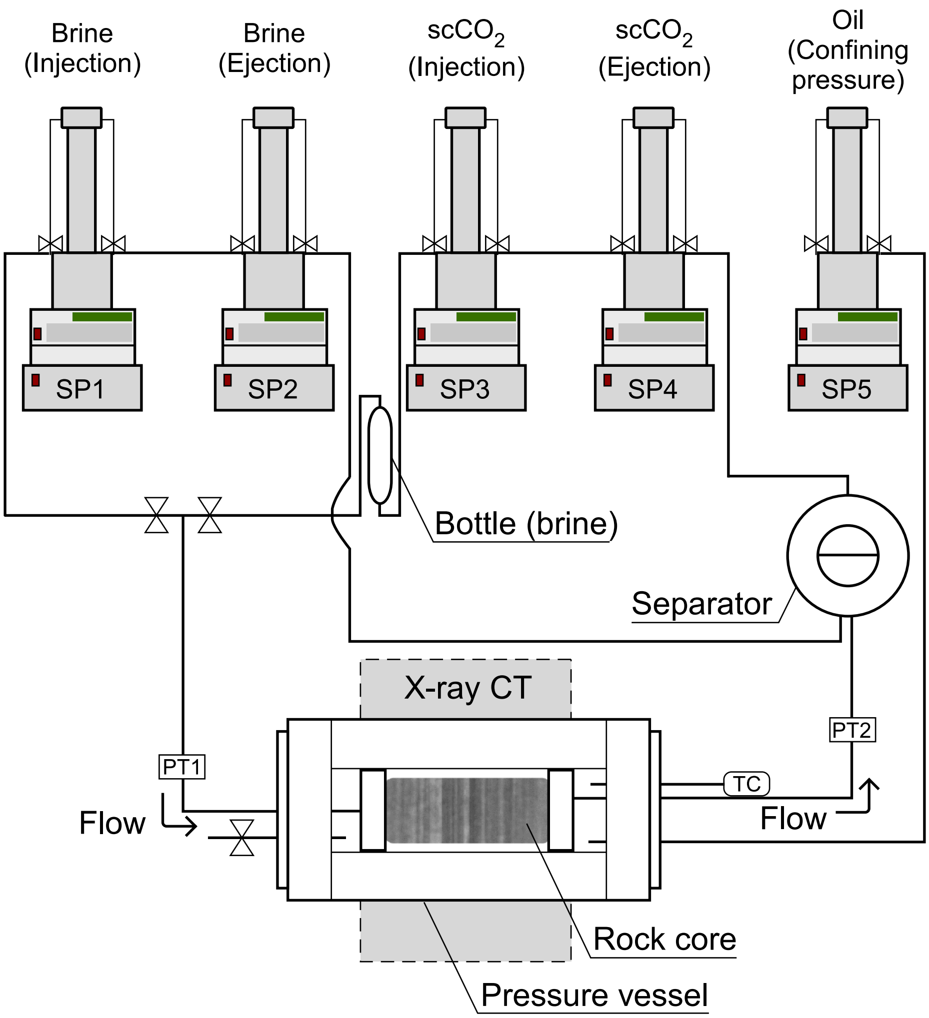

Figure 2. A schematic of the fluid line. The abbreviations 'SP', 'PT' and 'TC' stand for syringe pump, pressure transducer and thermocouple, respectively. (Colour in online-only publication).

injection porosimetry on a Berea sandstone core which was sampled from the same rock mass as our sample. The porosimetry revealed that the total porosities of low- and high-density layers are 19.5 per cent and 14.6 per cent, respectively, and the pores range from approximately 4–15 μm in the pore bodies to approximately 0.1–5 μm in the pore throats. The high-porosity layers contain a larger number of pore throats than the low-porosity layers; in other words, pore bodies in high-porosity layers are surrounded by more pore throats compared to low-porosity layers. Fig. 1 shows an image of a lateral section and the average porosity profile along the core axis. CT values within the 5 mm range from both ends of the core were removed because of uncertainties in CT image, due to the shadows of the guard collar and the boundary artefacts near the border between sample and end pieces. Porosity and saturation data in the axial distance range of 5–65 mm are employed here. The image was taken by scanning the horizontally laid core with a medical X-ray CT scanner (see Section 2.2 for details). Grey-scale values reflect the degree of X-ray attenuation: light and dark grey corresponds to high and low attenuation, respectively. Since Berea sandstone is composed almost entirely of quartz, the degree of X-ray attenuation shown by the grey scale of the image corresponds well to porosity (i.e. light and dark colours correspond to low- and high-porosity layers). High- and low-porosity layers are denoted as HPL and LPL, respectively. Macroscopic flow direction was almost perpendicular to the layers.

2.2 Flow and imaging apparatus

Fig. 2 shows our experimental system. We used a polyamide-imide (a high-tensile-strength plastic) cylinder as a pressure vessel with inner and outer diameters of 50 and 100 mm, respectively. Both ends of the cylinder were sealed and the inside of the cylinder was pressurized with oil. The lateral surface of the cylinder was wrapped with a carbon-coated heater and aramid fibre to provide heat to the pressure cylinder and maintain X-ray transparency.

Flow rate, and pressure of brine and CO_2 were controlled by syringe pumps (Teledyne ISCO, 500D, SP1–4 in Fig. 2). Brine and CO_2 were injected into the core using SP1 and SP3, respectively. The ejected fluid from the core was separated into brine and CO_2 by a separator. The separated brine and CO_2 were again recharged into SP2 and SP4, respectively. Syringe pump 5 was used to control confining pressure. Pressure transducers (PT1 and PT2 in Fig. 2) were used to monitor differential pressure across the core. Mean fluid pressure was about 10 MPa. The flow rate, pressure and volume of fluids were recorded throughout experiment. The temperature inside the pressure vessel was measured by a thermocouple (TC in Fig. 2).

Assembled parts in the fluid-flow system were heated to keep CO_2 in a supercritical phase. All syringe pumps were located inside a heat insulation box made of Styrofoam. The inside of the box was kept at 40 °C by a water bath circulator. Flexible heaters were applied to the separator, the bottle and the lines for fluids to keep the temperature constant at 40 °C. Hereafter, the term 'CO_2'that is associated with the present experiment is referred to as the supercritical CO_2, unless otherwise noted.

A medical X-ray CT scanner (Aquilion ONE TSX 301A, Toshiba Medical Systems Corp.), operated at 120 kV and 150 mA, was used to image the core. It has a high-speed helical scan system allowing fast acquisition of snapshot images of the fluid flow. Each whole sample scan requires one second. In each scan, image sections with 512 × 512 pixels for each 40 mm × 40 mm core section were reconstructed with a 0.5 mm interval between sections. A total of 160 sections perpendicular to the axis were acquired for each scan. The size of each voxel (in 3-D) is 0.078 × 0.078 × 0.5 mm.

2.3 Sample assemblage and preparation protocol

The rock core and end pieces were wrapped with thermal shrinking film made of polyethylene terephthalate (PET), and covered with polyvinylidene chloride (PVDC: known as SARAN resin, a trademark of Dow Chemical Inc.). An index showing CO_2 diffusivity per pressure for PET and PVDC at 25 °C are 7–11 × 10^{-19} (Azo materials 2003a) and 2 × 10^{-19} in the unit $m^2\ s^{-1}\ Pa^{-1}$ (Azo materials 2003b), respectively. It is known that PVDC is the strongest gas barrier material. A coating of PVDC was made by painting a water emulsion of PVDC (SARAN latex). The sample assemblage, SUS316 end pieces and guard rings, is coated with elastic adhesive (EP001, CEMEDINE Co. Ltd). We monitored the volume of SP5 to verify the efficiency of the sample coating against CO_2 leakage. If CO_2 had leaked out from the core to the hydraulic oil through the coating materials, the volume of the SP5 syringe would have shown a continuing increase during experimental runs. The SP5 syringe volume indicated almost no leakage during whole experimental runs continued for about two weeks.

2.4 Injection experiments

To enhance the contrast in X-ray CT images between water and CO_2, potassium iodide (KI, 12.5 wt. per cent) was added to pure water as a contrast medium. This fluid was then saturated with CO_2. Hereafter, the term 'brine' refers to the CO_2-saturated KI solution. The fully CO_2-saturated brine was prepared by mixing brine and CO_2 in a pressurized tank under the same temperature and pressure conditions as the sample vessel. The prepared CO_2-saturated brine was set in SP1. Carbon dioxide was also saturated with brine by passing it through a bottle filled with brine, connected to SP3. Carbon dioxide and brine were mixed with each other by passing simultaneously through the T-connection of the stainless steel tube.

Injection runs are labeled D1 through D6 (Table 1). In all injection runs except the end-member injection run D6, mixtures of brine and CO_2 were injected simultaneously. Before the start of the first drainage, D1, the core had been brine-saturated. Injection was continued until the differential pressure between the inlet and outlet became stable. Local CO_2 saturation was monitored intermittently by converting the core image to a CO_2 saturation map using equations described in the next section. The monitoring interval

Table 1. Summary of observations.

	Flow rate (mL min^{-1})			Injected volume (mL)			S_b (per cent) Entire core (d = 5–65 mm)	S_{CO2} (per cent)	S_b (per cent) Stuck zone (d = 5–25 mm)	S_{CO2} (per cent)	S_b (per cent) Normal-flow zone (d = 25–65 mm)	S_{CO2} (per cent)			
Run no.	Brine	CO_2	Total	Brine	CO_2	Total							ΔP (kPa)	k_{rb}	k_{rCO2}
D1	0.45	0.05	0.50	473.9	56.8	530.6	63.4	36.6	59.3	40.7	65.4	34.6	88.3	0.130	0.001
D2	0.35	0.15	0.50	343.0	149.6	492.6	60.9	39.1	57.6	42.4	62.6	37.4	99.6	0.090	0.002
D3	0.25	0.25	0.50	340.8	340.2	681.0	57.4	42.6	53.9	46.1	59.2	40.8	84.8	0.075	0.005
D4	0.15	0.35	0.50	412.9	961.0	1373.9	56.9	43.1	51.7	48.3	59.6	40.4	55.5	0.069	0.010
D5	0.05	0.45	0.50	63.5	546.5	610.0	52.2	47.8	46.6	53.4	55.0	45.0	35.2	0.036	0.020
D6	0.00	0.50	0.50	0.0	452.9	452.9	44.9	55.1	36.8	63.2	49.1	50.9	6.7	0.000	0.116

Note: d = Distance from inlet side of the core.

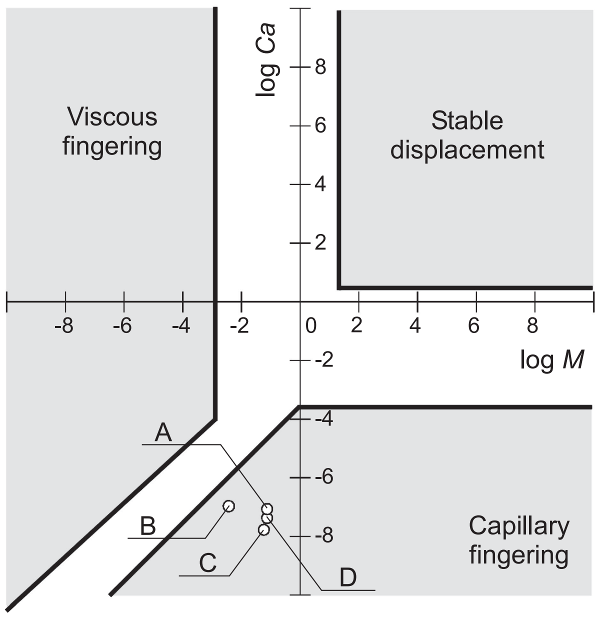

Figure 3. A drainage phase diagram proposed by Lenormand *et al*. (1988). Displacement flow is classified into three types: stable displacement, viscous fingering and capillary fingering, depending on the logarithms of capillary number, C_a and the viscosity ratio between displacing and displaced phases, *M*. Plotted circles show the conditions of relative permeability measurements with fluid velocity less than 1.65×10^{-5} m s^{-1}: A = this study; B = Perrin & Benson (2010); C = Akbarabadi & Piri (2013); D = Kogure *et al*. (2013).

becomes shorter when approaching the stable state. After reaching a steady-flow state, the flow rates of brine and CO_2 were changed. Subsequent injections were performed by decreasing the volume ratio of brine to CO_2. The ratios between brine and CO_2 were 9:1, 7:3, 5:5, 3:7, 1:9 and 0:10. Table 1 lists flow rate, total injected volume and the ΔP at the end of each measurement run calculated from linear-regression approximations for the data 3–5 hr before the end of injection runs (Fig. 7). Saturation values, S_b and S_{CO2}, are the time-averaged values for 2 hr before end of injection.

Confining pressure was set at 12 MPa for all injection runs. Injection pressure was set at 10 MPa, and backpressure changed depending on CO_2 flow rate and saturation states of the core. When starting injection, the backpressure was decreased slightly to generate the differential pressure necessary for maintaining a constant flow rate. While keeping a constant fluid flow rate, injection of brine and CO_2 was continued until the flow in the core became steady.

2.5 Capillary number and flow rate

Lenormand *et al*. (1988) showed a drainage diagram in which non-wetting fluid displaces wetting fluid (Fig. 3). Displacement flows are classified into three types according to their flow-pattern geometry: stable displacement, viscous fingering and capillary fingering. These depend on the capillary number of flow, C_a and the viscosity ratio of two phases, *M*. Regions of the three flow patterns are plotted on a diagram of the two common logarithms of C_a and *M*. The combination of log C_a and log *M* in this study falls in the 'capillary fingering' domain, similar to Perrin & Benson (2010), Akbarabadi & Piri (2013) and Kogure *et al*. (2013), where fluid velocities were less than 1.65×10^{-5} m s^{-1}. In our experiments, total flow velocity of brine and CO_2 was set at 8.67×10^{-6} m s^{-1}. Therefore, according to the classification by Lenormand *et al*. (1988), capillary-dominated flow is the principal mechanism of displacement flow in our study.

A flow velocity of 1.65×10^{-5} m s^{-1} corresponds to the fluid velocity that would be expected for a large CO_2 storage project in the region around the injection well (e.g. Perrin & Benson 2010). Many previous measurements were conducted with higher two-phase flow velocities (i.e. larger capillary number) than the present experiment, which can only mimic flow near the injection well. With the exception of Akbarabadi & Piri (2013), Kogure *et al*. (2013) and one measurement from Perrin & Benson (2010), fluid velocities were almost equal to, or larger than, 1.65×10^{-5} m s^{-1}.

3 DATA ANALYSES

3.1 Estimation of porosity and saturation

Fluid flow inside the core can be characterized by analysing X-ray CT images. The digital CT number (Hounsfield number) describes the intensity of the X-ray attenuation in a small volume (voxel) inside the core. When a sandstone core is saturated with the KI brine solution, high porosity voxels will show large X-ray attenuations (high CT numbers) due to the high-KI content in the voxel, and low porosity voxels will exhibit lower attenuations (low CT numbers). The following equations yield the voxel porosity, ϕ, and the degree of CO_2 saturation, S_{CO2}, based on voxel CT numbers (Akin & Kovscek 2003):

$$\phi = \frac{CT_{brine}^{sat} - CT^{dry}}{CT_{brine} - CT_{air}}, \quad (1)$$

$$S_{CO2} = c\left(CT_{obs} - CT_{brine}^{sat}\right) = \frac{CT_{obs} - CT_{brine}^{sat}}{CT_{CO_2}^{sat} - CT_{brine}^{sat}}, \quad (2)$$

where CT_{brine}^{sat}, $CT_{CO_2}^{sat}$, CT^{dry} and CT_{obs} are the voxel CT numbers of a scanned rock which is saturated with brine, CO_2, vacuumed and other conditions observed during the scan, respectively. CT_{brine} and CT_{air} are the CT numbers for the single brine or air phase, respectively, and c is the coefficient that relates S_{CO2} to the difference in CT number between the scan for the experimental run in question and the scan run for the brine-saturated core.

3.2 Calculation of relative permeability

Relative permeability is calculated using Darcy's law:

$$Q_i = -\frac{A k_{abs} k_{ri}}{\mu_i}\frac{\Delta P}{L} \quad (i = \text{brine or } CO_2), \quad (3)$$

where Q_i and μ_i are the flow rate (m^3 s^{-1}) and the viscosity (Pa·s) of each fluid, $k_{abs}$and k_{ri} are the absolute permeability (m^2) and the relative permeability, A and L are the sectional area (m^2) and the length of the core (m), and ΔP is the differential pressure across the core (Pa).The values of μ_b and μ_{CO_2} at 40 °C and 10 MPa are 6.53×10^{-4} Pa·s (Kogure *et al*. 2013) and 4.78×10^{-5} Pa·s (Span & Wagner 1996), respectively.

Pini & Benson (2013) and Krause & Benson (2015) used the capillary-pressure gradient in CO_2 when calculating the CO_2 relative permeability. However, we use observed ΔP in the same manner as Reynolds & Krevor (2015) in eq. (3), ignoring capillary-pressure gradient in CO_2. We consider that the CO_2 saturation values in rock do not necessarily reflect the local CO_2 capillary pressures in two-fluid flow conditions. Recent micro CT experiments have revealed that some amount of CO_2 exist as disconnected ganglia (Andrew *et al*. 2013; Al-Menhali *et al*. 2016). Those CO_2 ganglia can exist with capillary pressures different from those in connected pathways. The unique relationship between CO_2 saturation and capillary pressure exists only in connected pathways where CO_2 moves due to the capillary-pressure gradient of CO_2. Ganglion dynamics include snap off of connected pathways and coalescences of ganglia (Andrew *et al*. 2015), causing morphological changes in connected CO_2 pathways. It is unreasonable to expect a unique relationship between local CO_2 capillary pressure and local CO_2 saturation during the two-fluid flow of brine and CO_2.

We also ignored the capillary end effect that appears as the offset pressure in the measured capillary-pressure difference. The capillary end effect is caused by capillary entry pressure when the measured pressure at outlet is the pore pressure. If the measured pressure at the outlet is the CO_2 pressure, the capillary entry pressure does not exist; this corresponds to the case of one-fluid drainage (i.e. CO_2 drainage). In any case, the corrections due to capillary entry pressure in Berea sandstone, *ca*. 5–6 kPa (Pini & Benson 2013), are considered to be small compared to the observed pressure differences, 35–100 kPa.

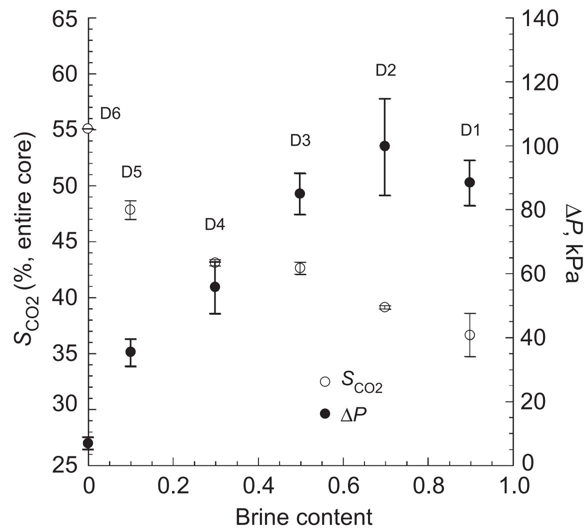

Figure 4. Steady-state CO_2 saturation values (S_{CO2}) and differential pressure between inlet and outlet of the core (ΔP) with respect to injected brine volume ratio listed in Table 1. All experimental runs were conducted at constant flow rate of 0.5 mL min^{-1}. D1–D6 correspond to those in Table 1. Each bar shows the range of 1σ for both S_{CO2} and ΔP.

4 CHARACTERISTICS OF FLUID FLOW

4.1 General characteristics of channel pathway and randomly distributed pathway

Armstrong *et al*. (2016) pointed out two important elementary processes in concurrent flow of non-wetting and wetting fluids in porous rock. One is the mutual displacements of wetting and non-wetting fluids in pores and the other is non-wetting fluid flow through connected pathways. The former is called ganglion dynamics of which important mechanisms are coalescences of non-wetting ganglia and their snap off. The latter is related to realization of percolation clusters of non-wetting fluid which connect the inlet and outlet ends of core sample. When random pore networks exist in a porous medium, there is a threshold value for the non-wetting fluid saturation above which connected pathways of non-wetting fluids always exist between inlet and outlet ends (Stauffer & Aharony 1994).

Ganglion dynamics is important when CO_2 is first injected into a rock already saturated with brine. When the pressure in a CO_2 ganglion exceeds the capillary pressure of a pore throat, CO_2 can move toward the low-pressure region. When there are large-pore zones, fractures, or joints in a rock sample, the capillary pressure in such zones will be lower than the surrounding area. Carbon dioxide preferentially moves into such low capillary-pressure zones and forms large CO_2 ganglia. When these kinds of large ganglia appear, the pressure difference due to capillary pressure is mitigated inside the ganglia. Carbon dioxide moves inside ganglia following Darcy's law where the viscosity of CO_2 and pathway width play roles. When the large ganglia concentrate and unevenly distribute in a core, this is referred to as 'channel', hereafter. The channels work as efficient flow pathways for CO_2 flow, compared to ganglion dynamics under similar internal pressure gradients.

There will also be an ensemble of randomly distributed connected pathways (referred to as 'random pathway', hereafter) in sandstones (Reynolds & Krevor 2015). A typical random pathway consists of connected pathways of small ganglia. The boundary between channel flow and random pathway is not clear, and both can coexist in a core. In an X-ray CT image, a channel is characterized as a strong contrast of CO_2- and brine-rich zones. Randomly distributed pathways may become channel flow paths as CO_2 pervades pore networks, with increasing of CO_2 saturation in a core. Channels and random pathways are formed depending on internal structure of core, especially inhomogeneity of grain- and pore-size distributions. Introducing the two pathway model extremes will help to understand CO_2 movement in porous media. We describe interplay of the two flow types in CO_2 drainage during concurrent CO_2/brine injections.

Fig. 4 shows relationships of the S_{CO2} averaged over the entire core and the ΔP at the end of each measurement run with respect to injected brine content (Table 1).Values for ΔP were calculated from linear-regression trends obtained from the data close to the steady-flow state (Fig. 7).The bars indicate 1σ ranges of ΔP and fluctuations in axial profiles of S_{CO2}. The differential pressure ΔP first increased between runs D1 and D2, and then decreased as the brine content of the injected fluid decreased. Saturation of CO_2 increased from runs D1 to D6, up to 55 per cent in run D6 where only CO_2 was injected.

There are three different kinds of flow stages in the present drainage runs: (1) D1, (2) D2–D5 and (3) D6. D1 is two-fluid injection into brine saturated rock. Runs D2–D5 are two-fluid injection into partially CO_2 saturated rock. Run D6 is a single end-member (CO_2) injection into the partially saturated rock.

4.2 From unsteady flow to steady flow in run D1

The time variation in differential pressure, ΔP, during run D1 is shown in Fig. 5, together with a CT image of dried core and selected sectional S_{CO2} distribution maps along the core axis (S_{CO2} axial profile) and in LPL sections perpendicular to the axis. The differential pressure increased from 2 to 5 hr. Then, the syringe of SP3 was refilled with CO_2. During the refill, injection was interrupted and the differential pressure was raised to prevent counter flow inside the sample (discontinuity in ΔP). After recommencement of injection with the same flow rate, the differential pressure was maintained, suggesting that the pause of injection caused no disturbance for the measurement. A steep increase of pressure started at the lapse time 2 hr and continued only for 1 hr. The flection in ΔP corresponds to formation of a channel flow at the upper part of the core (centre of the bottom panel) which appeared to circumvent the LPL located

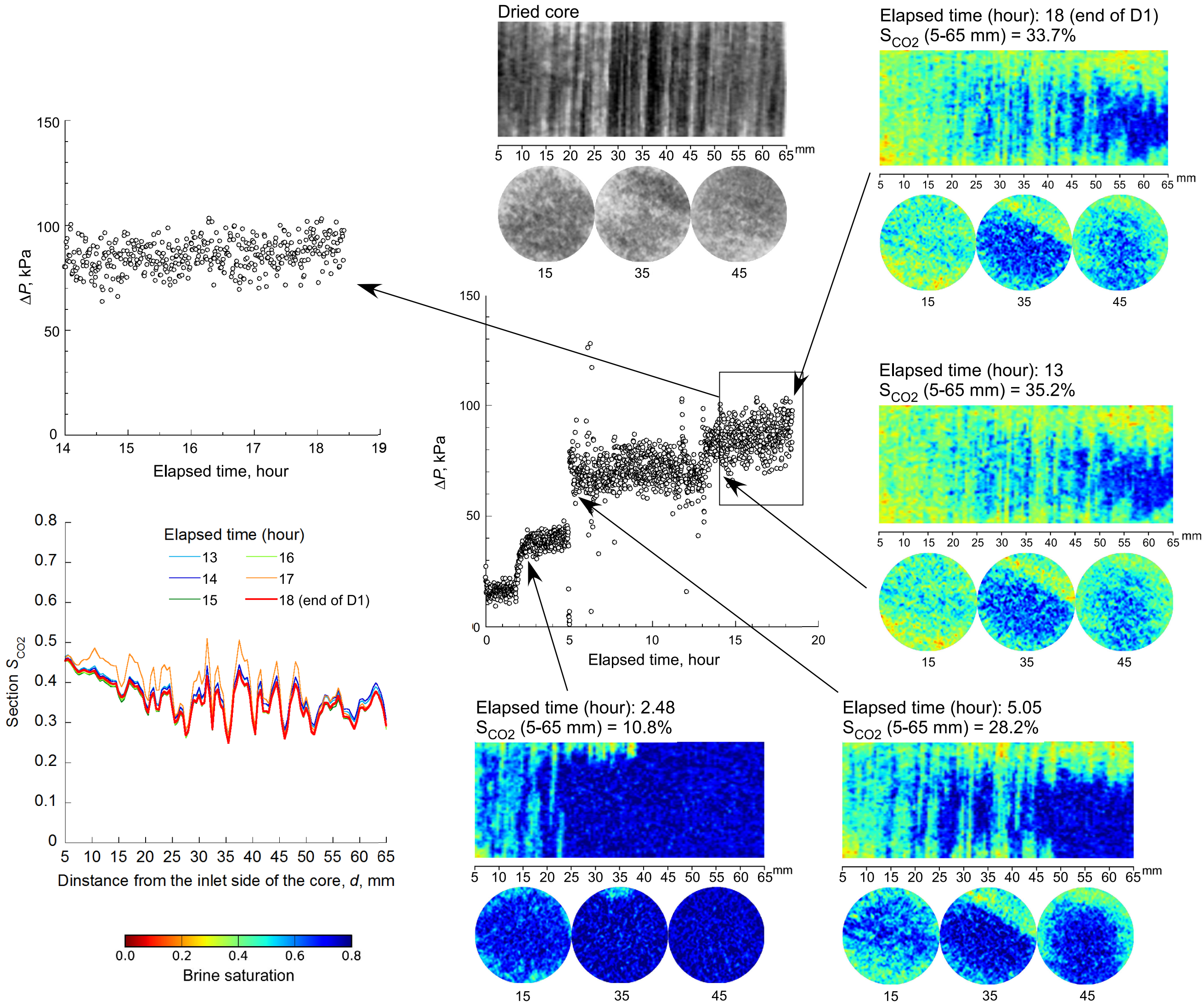

Figure 5. Time variations of differential pressure across the core, ΔP, together with saturation maps of brine and sectional S_{CO2} profiles along the long axis during the injection of CO_2 in run D1. The dried core image is included to show the layered inhomogeneity. (Colour in online-only publication).

at 25–27.5 mm. The layer worked as a strong barrier against CO_2 flow.

The differential pressure showed considerable fluctuations. Outliers in ΔP appeared in both positive and negative directions during the lapse time 5–13 hr. This may reflect influences from ganglion dynamics. Experiments by Tallakstad *et al.* (2009) revealed avalanche-like flow in air–water flow. When air ganglia were blocked out by water, pressures of air ganglia increased and gradually pushed blocked water. Sometime after, an avalanche of expanding air was triggered. The avalanche formed a large channel that extended widely, and pressures in the channel suddenly dropped. Similar avalanches may have appeared in the present CO_2/brine flow because there is a large difference in compressibility between CO_2 and brine. If the new avalanche channel connects to existing CO_2 flow channels and the size of the new channel is large, a large pressure drop is expected and the change in differential pressure can be measured. Armstrong *et al.* (2016) and Tallakstad *et al.* (2009) pointed out that the size of non-wetting ganglia becomes large as the capillary number decreases. The small capillary number of the present experiment raises expectations that the changes in differential pressure were caused by avalanche-like flow of CO_2 because of larger sizes in CO_2 ganglia. The outliers may be in association with an accumulation and abrupt drop of pressure before and after an avalanche.

The fluctuation in ΔP is intrinsic to the steady state as demonstrated by Tallakstad *et al.* (2009) for a homogeneous porous medium. In the present experiment, a small step increase in ΔP accompanied by negative and positive outliers appeared at the elapsed time of 14 hr. After this time, outliers disappeared and steady networks are assumed to have been formed.

The saturation maps show a trend that S_{CO2} is higher near the inlet end than near the outlet end. This is primarily due to the capillary-pressure gradient of CO_2 associated with the differential pressure. In addition to this trend, S_{CO2} was higher in HPL than in LPL, generating S_{CO2} contrasts at repeating alternate layers. As mentioned above, there was a small-scale channel at the upper part of the core. Carbon dioxide first moved through this small-scale channel but the channel capacity was too small to maintain whole CO_2 flow. Increase of S_{CO2} leads to formation of percolated pathways inside each HPL, which can be regarded as large ganglia. The small channel connecting the inlet and outlet would connect to CO_2 ganglia pervaded in HPL. Some connected pathways seemed to

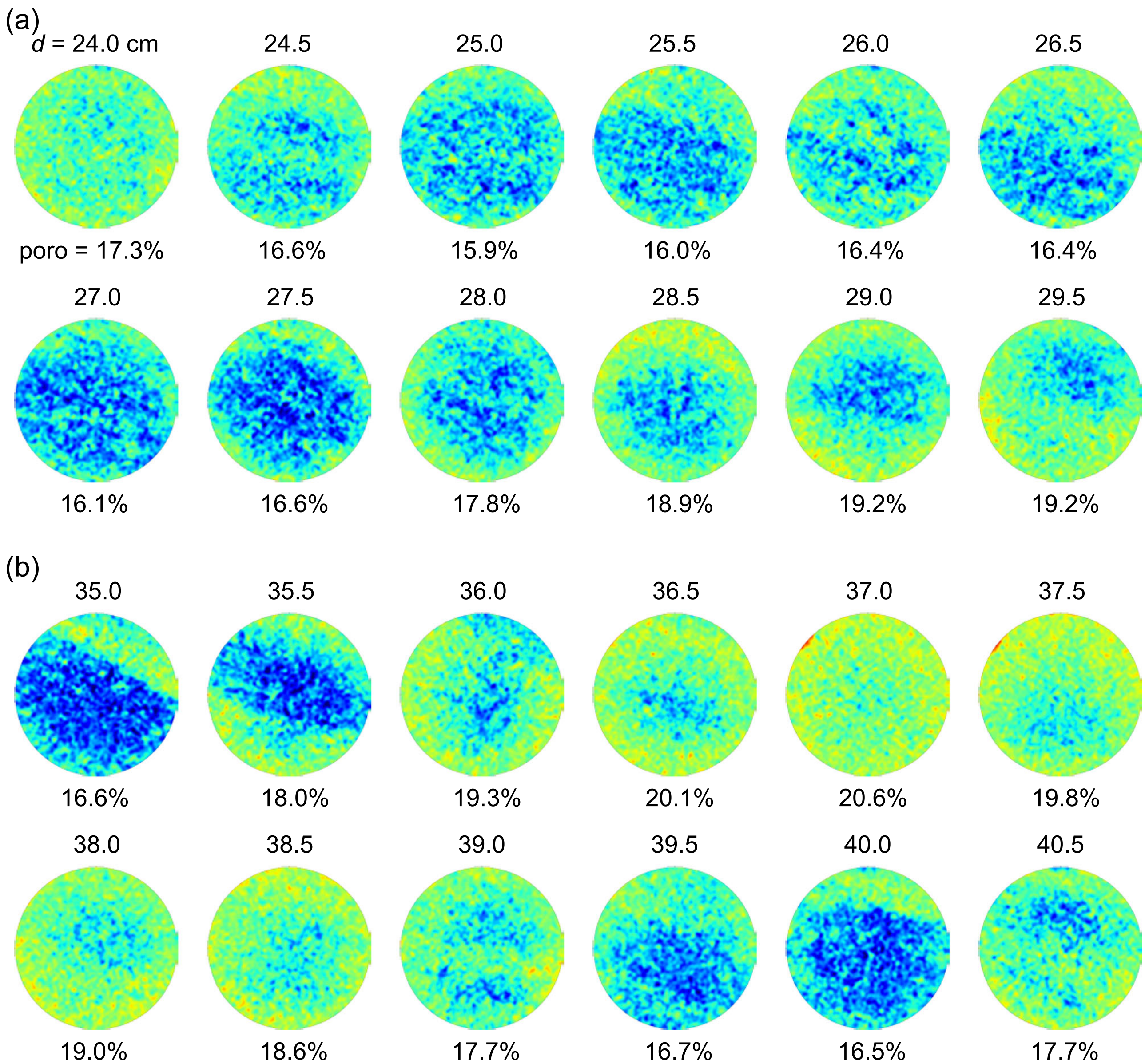

Figure 6. Sectional S_{CO2} distribution along the long axis at the end of run D1 (a) $d = 24.0$–29.5 mm and (b) $d = 35.0$–40.5 mm. The distances from inlet side of the core and the averaged sectional porosity are shown for each distribution map. Colour scale is the same as shown in Fig. 5. (Colour in online-only publication).

exist in LPL, other than the small channel mentioned above. Those pathways in LPL will connect to HPL and create new percolated pathways through LPL. The percolated pathways that connect inlet and outlet would be created. Most of the pathways in LPL were randomly distributed. The basic skeleton of flow paths in steady state of run D1 consisted of the small-scale channel at the upper part and the randomly distributed pore network in LPL that connected the neighbouring HPL.

Fig. 6 shows sectional S_{CO2} maps at the end of run D1. The yellow coloured pixels indicate probable areas for pathway. Pathway is distributed randomly over the entire section in HPL at 24 mm (make correction: the figure and caption say cm, not mm) in Fig. 6(a), then, the pathways became biased toward the upper part of the sections at 24.5–27.5 mm, which belong to LPL. Since the layers lean slightly towards the outlet side, a part of HPL appears at the upper side of LPL as shown in the section at 35 mm in Fig. 6(b). Pathway distributed randomly in HPL (centred at 37 mm). Channels mainly appeared at the upper part of sections in all the saturation maps in Fig. 6. Flow paths of the steady state consisted of small-scale channels and an ensemble of randomly distributed pathway.

4.3 Steady-state flow in runs D1–D5

4.3.1 Differential pressure

Fig. 7 shows time variation of the differential pressure, ΔP, for 5 hr before the end of injection in all the measurements. A linear-regression equation was obtained in each graph. The equations show slight increasing trends in ΔP in runs D1 and D2, suggesting that steady-state flow has not been completely achieved. When the flow rate of CO_2 is small, it seems to take much time to achieve a complete steady-flow state. Approaching a steady state

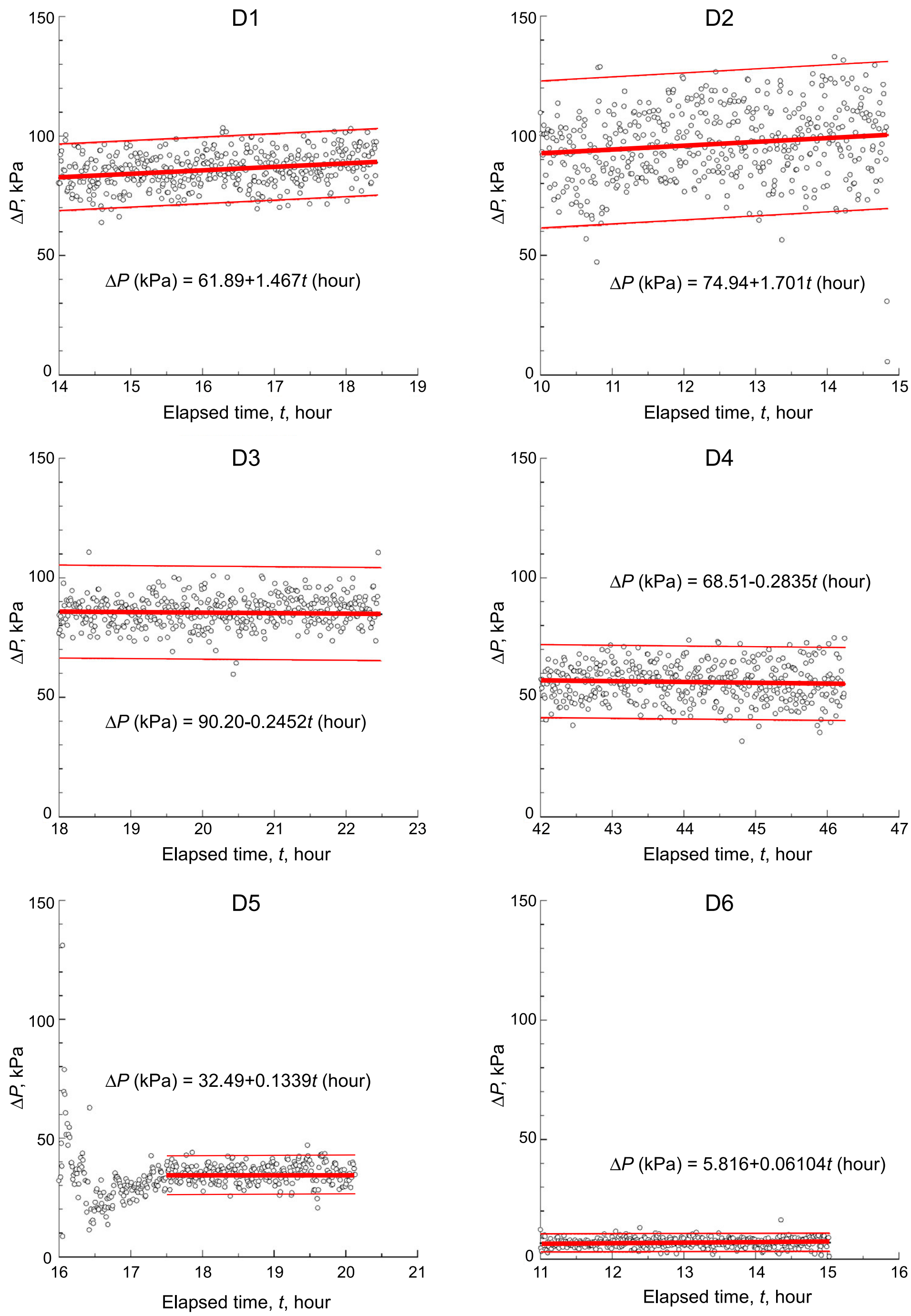

Figure 7. Time variation of ΔP for 5 hr before the end of injection in all injection runs. There seem to be linear trends and random fluctuations as shown by the linear regression and 2σ shown by the thick and thin lines. We used the ΔP at the final value of the linear regression for all calculations in Table 1 and Figs 4 and 15. (Colour in online-only publication).

may be logarithmic in time, in which case small increasing ΔP trends in runs D1 and D2 allow one to regard the linear-regression ΔP at the end of injection to be close to the values at steady states.

Fluctuations appeared in ΔP depending on the volume fractions of CO_2 in flow. Fluctuation amplitude was the largest in run D2 and it gradually decreased as drainage proceeds. The change may be associated with the flow mechanism. Armstrong *et al.* (2016) pointed out that the flow mechanism of non-wetting fluid changes from ganglion dynamics to connected-pathway flow with increasing of saturation of non-wetting fluid. Ganglion dynamics may prevail in run D2 when random connected pathways were formed. The connected pathways are easily snapped off by brine because CO_2 blobs frequently connect (coalescence) and disconnect (snap off by brine) with each other when a considerable volume of brine flow still coexists (Armstrong *et al.* 2016). The coalescence and snap off is accompanied by pressure increase and drop, respectively (Berg *et al.* 2013). Therefore, the large fluctuation in ΔP may reflect the predominance of ganglion dynamics compared with pathway flow. Both flow regimes coexist over a wide range of

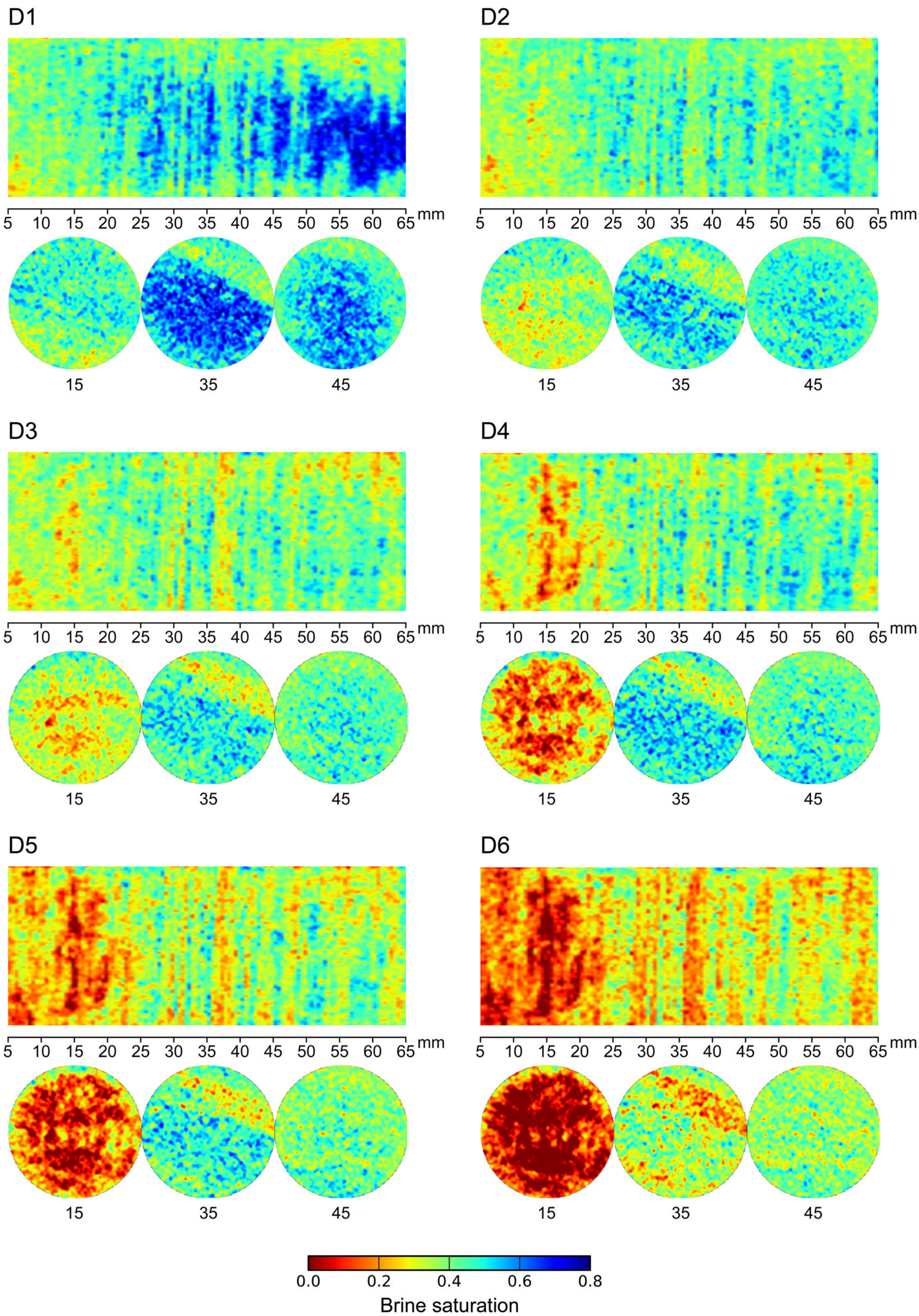

Figure 8. Saturation map of brine. Fluids were injected from the left-hand side. Each image was taken just before the end of the injection. The upper edge of each image show physical top edge of the core. (Colour in online-only publication).

saturation, $50 < S_b < 75$ per cent, and flow rate (capillary number) without a sharp transition between the regimes (Armstrong *et al.* 2016). If the same properties appeared in a CO_2–brine flow case, the brine saturation values for the steady flow in runs D1–D5 correspond to the coexisting regime of the two mechanisms. The value of ΔP and its fluctuations decreased from runs D2 to D5, suggesting domination of connected-pathway flow with increasing of S_{CO2}.

4.3.2 Saturation map and axial CO_2 distribution

Fig. 8 shows saturation maps at the end of injection, the moment when steady-state flow was achieved. The saturation is illustrated as one rectangular map including the axis (upper panel), and three slices at different locations along the axis (lower panel). The distribution of CO_2 reflects the sedimentary structure of the rock, which is characterized by layered differences in porosity (HPL and LPL in Fig. 1). Carbon dioxide was predominant in HPL because of the smaller capillary-pressure threshold in HPL.

There was a high CO_2 saturated zone from the inlet to the distance 25 mm. The high saturation zone became remarkable as CO_2 flow fraction increased. This high saturation zone was generated from the blocking of CO_2 flow by the LPL located at 25 mm (Fig. 1). We accordingly separate the core into two zones at $d = 25$ mm, by referring to these as a stuck zone and a normal-flow zone for $5 < d < 25$ mm and $25 < d < 65$ mm, respectively.

In the saturation map for run D1, brine-rich areas remain in the normal-flow zone. The map suggests a channel at the upper part of the core in the steady-flow state. The brine-rich areas behaved as a barrier for CO_2 flow, and CO_2 mostly flowed through the channel. In run D2, the brine-rich zones were narrowed, and some parts in LPL reached 40 per cent CO_2 saturation (light green). The saturation value of percolated path formation in pore networks has been estimated as 35–40 per cent for most sandstones from electrical conductivity measurements (Argaud *et al*. 1989; Han *et al*. 2009). It is therefore highly possible that the continuing green-yellow voxels in LPL work as percolated pathways that connect neighbouring HPL. The connected pathways in LPL were distributed randomly as indicated by section images at 35 and 45 mm (Fig. 7). The randomly distributed network would have been formed in both HPL and LPL by connected pathways in LPLs. The pathways would have enough capacity for the CO_2 flow (0.15 mL min^{-1}). At the same time, there would be many opportunities that concurrent flow of brine can snap off the percolated pathways in LPL. This may have caused more pressure fluctuations.

Carbon dioxide was concentrated near the injection side during runs D3 and D4, in which CO_2 saturation reached 46–48 per cent. The average S_{CO2} in the normal-flow zone was almost equal for runs D3 and D4 (40.8 per cent and 40.4 per cent), although the total amount of injected CO_2 in run D4 was twice as large as that in run D3 (1373.9 and 681 mL, respectively, Table 1). We try to interpret the similar values in S_{CO2} in the normal zone of runs D3 and D4 on the basis of a simple classical percolation model. If the value of S_{CO2} represents the occupation probability of site or bond percolation, the realization probability of percolated cluster increases drastically just slightly over the percolation threshold (e.g. Hoshen *et al*. 1979). This suggests that the similar values appear in S_{CO2} even for different fraction of CO_2. The average S_{CO2} over whole core, stuck zone and normal-flow zone increased in run D5. The maximum CO_2 saturation was attained in run D6, with large S_{CO2} in the stuck zone.

Fig. 9 shows the axial S_{CO2} profile which covers the 2 hr period prior to the end of injection. The axial S_{CO2} profile became constant in run D6 because almost all CO_2 can flow through connected pathways during the single-phase injection of CO_2 without snap off by brine. The axial profile for run D2 also became constant although the axial profiles for the other multiphase injection run showed fluctuation. There may be a relationship between the fluctuation in ΔP and pathway formation, random or channel. However, detailed mechanisms relating the fluctuation in pressure with that in the axial S_{CO2} profile is not clear at this moment.

Fig. 10 shows axial profiles of S_{CO2} for the runs D1–D6, together with the axial porosity profile. Porosity seems to be uncorrelated with S_{CO2} in the stuck zone ($d < 25$ mm) as indicated by thin lines LPL1 and HPL1, but it is well correlated with S_{CO2}in the normal-flow zone (25 mm $< d <$ 65 mm) as indicated by LPL2–HPL3. To see the correlation in detail, values in profiles were cross-plotted for the stuck zone (Fig. 11a) and the normal-flow zone (Fig. 11b). In the stuck zone, the correlations are weakly positive for runs D1–D3, but not clear for runs D4–D6 (Fig. 11a). In contrast to this, positive correlations are clear in the normal-flow zone for runs D1–D6 (Fig. 11b).

4.3.3 Saturation fluctuation dynamics

Armstrong *et al*. (2016) suggested that the ganglion-dynamics regime extends towards non-wetting fluid saturation as the capillary number decreases. Ganglion dynamics appears to be still working in runs D2–D4 ($S_{CO2} = 37$–40 per cent), although the main flow mechanism of CO_2 is connected-pathway flow through percolated ganglia. During the two-fluid injections, morphological changes occurred in the CO_2 percolated clusters by repeated ganglion coalescence and brine snap off as shown schematically in Fig. 12. The difference in morphology between HPL and LPL in Fig. 12 is characterized by the difference in pore throat aperture as Zhang *et al*. (2014) reported: total volume of large-aperture pore throat is larger in HPL than in LPL, although the radii of pore bodies are almost the same in HPL and LPL. To show the above condition in a 2-D square lattice, the frequency of wider pore throats is larger in HPL zone than LPL zone (Fig. 12). As a first approximation, we consider no anisotropy inside both layers, while anisotropic percolation can occur at the core scale, depending on the relationship between flow direction and the layering structure. In Fig. 12(a), a pore network connecting the left and right ends exists. When CO_2 starts to flow through this percolated pathway, ΔP decreases because of the quick movement of CO_2 due to its low viscosity and high compressibility. Brine then can invade through narrow pore throats where CO_2 pathways should be sustained with high capillary pressure (Fig. 12b). The CO_2 pathways become disconnected until rebuild up of CO_2 pressure by additional CO_2 accumulation in the pathway. After the re-formation of CO_2 percolation clusters, CO_2 moves again through the connected pathways. Creation of a percolation cluster again reduces CO_2 pressure. Each stage is illustrated in Fig. 13.

In their 3-D images of temporal oil and brine saturation distribution, Berg *et al*. (2016) concluded that the role of ganglion dynamics was minor. The proposed process (Fig. 13) of connection and disconnection of CO_2 pathways seems to be more efficient than the fluid movements by ganglion dynamics because the process does not include frequent displacements between CO_2 and brine. The action of ganglion dynamics within a limited small area can strongly affect the CO_2 transport through morphological changes in CO_2 pathways. Although fluctuations in pressure are small in runs D3, D4 and D5, the local S_{CO2} distribution still fluctuate in runs D3–D5 (Fig. 9). Disconnections in CO_2 pathways due to brine snap-off events cause the morphological change in connected CO_2 networks. The local S_{CO2} fluctuations in the high S_{CO2} stages suggest that the morphological change inCO_2 network is complicated, and causes the fluctuation in local S_{CO2} distribution. This viewpoint is supported by our differential pressure data and the local S_{CO2} in line

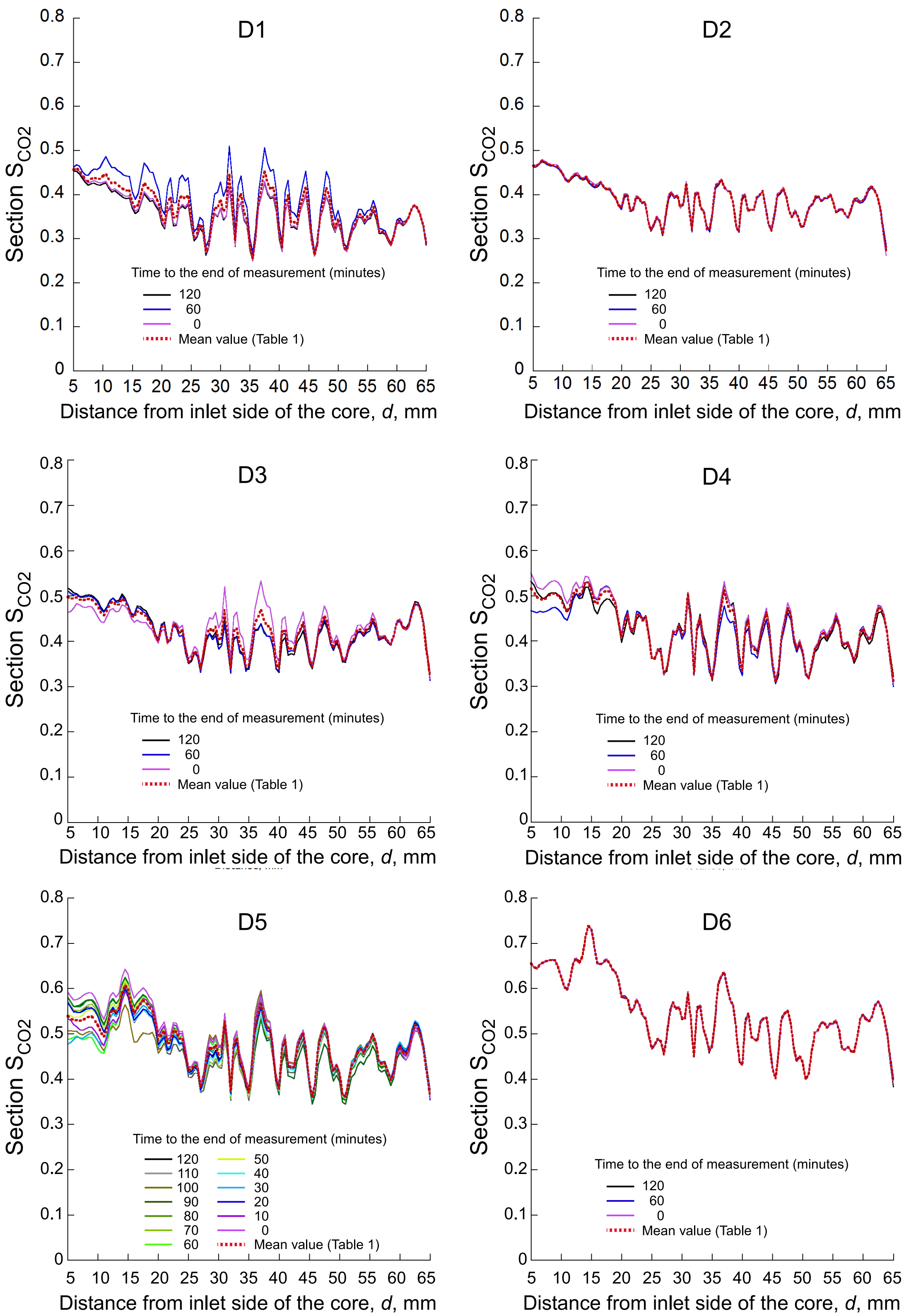

Figure 9. Temporal change in the axial S_{CO2} profile during the last 2 hr of runs D1–D6. (Colour in online-only publication).

with ganglion dynamics and percolation mechanisms of randomly connected pathways.

The local saturation of CO_2 fluctuated in the steady-flow state (Fig. 9), which occurred 2 hr prior to the end of injection. The saturation fluctuations were pronounced in HPL (Fig. 9) in runs D3–D5. Large fluctuations appeared within the CO_2 stuck zone in run D5. This may have been caused by the remnant CO_2 ganglia at the stuck zone due to the increase of CO_2 flow fraction in run D5.

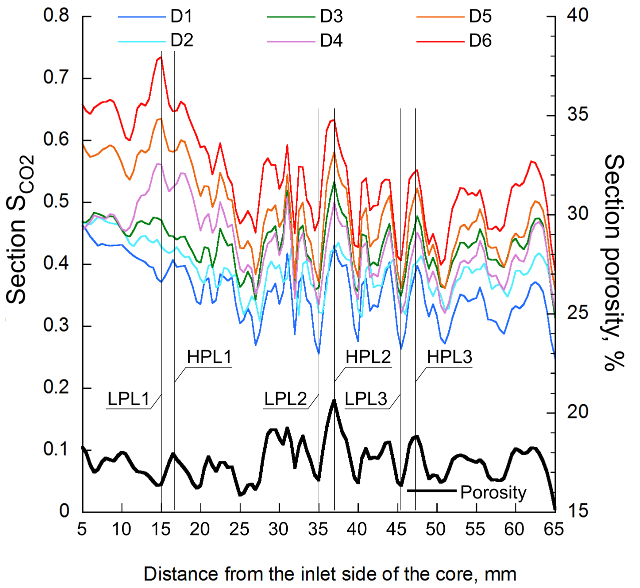

Figure 10. Axial S_{CO2} profiles in the six injection runs. Axial porosity profile is also shown. The sections denoted by LPL1–LPL3 and HPL1–HPL3 correspond to those in Fig. 1. (Colour in online-only publication).

4.4 Run D6

A distinctive contrast of the local S_{CO2} distribution between the stuck zone and the normal-flow zone appeared in run D6. The saturation map in Fig. 8 shows that CO_2 concentration in the stuck zone was due to the impermeable layer around $d = 25$ mm (Fig. 1). At the beginning of the injection run D6, CO_2 even invades into small pores in the stuck zone due to the accumulated capillary pressure produced by the high flow rate of CO_2. There is no significant correlation between section porosity and S_{CO2} in the stuck zone (Fig. 11a). However, there is a positive correlation between section porosity and S_{CO2} in the normal-flow zone (Fig. 11b). The high concentration of CO_2 in the stuck zone may be caused by the initial injection stage of run D6 due to the presence of the less permeable layer. This is a typical case which will be seen in CO_2 injections with small flow velocity, which accompanies small differential pressure across a core: no CT images like Fig. 8 have been reported in high flow-velocity measurements. When percolation pathways were created, the excess CO_2 was left in the stuck zone because the pressure drop in the pathways brings brine snap off. In the steady-flow state, the CO_2 dominated zone may be mainly the remnant CO_2 ganglia.

In run D6, ΔP was almost kept constant with very small fluctuations (Fig. 7), and S_{CO2} distribution was converged (Fig. 9). These suggest a completely connected-pathway flow in run D6 where displacement of brine by CO_2 due to ganglion dynamics scarcely occurred after reaching steady state. CO_2 keep flowing through the connected pathway having enough transportation capacity. Brine percolation clusters still exist in run D6 because the saturation value of brine still exceeds the value for percolation cluster formation, but no additional brine is injected. There was little to no brine flow in run D6, and therefore little chance for brine snap-off event. CO_2 migration in percolation cluster follows Darcy's law, showing much smaller pressure gradient than in ganglion dynamics flow.

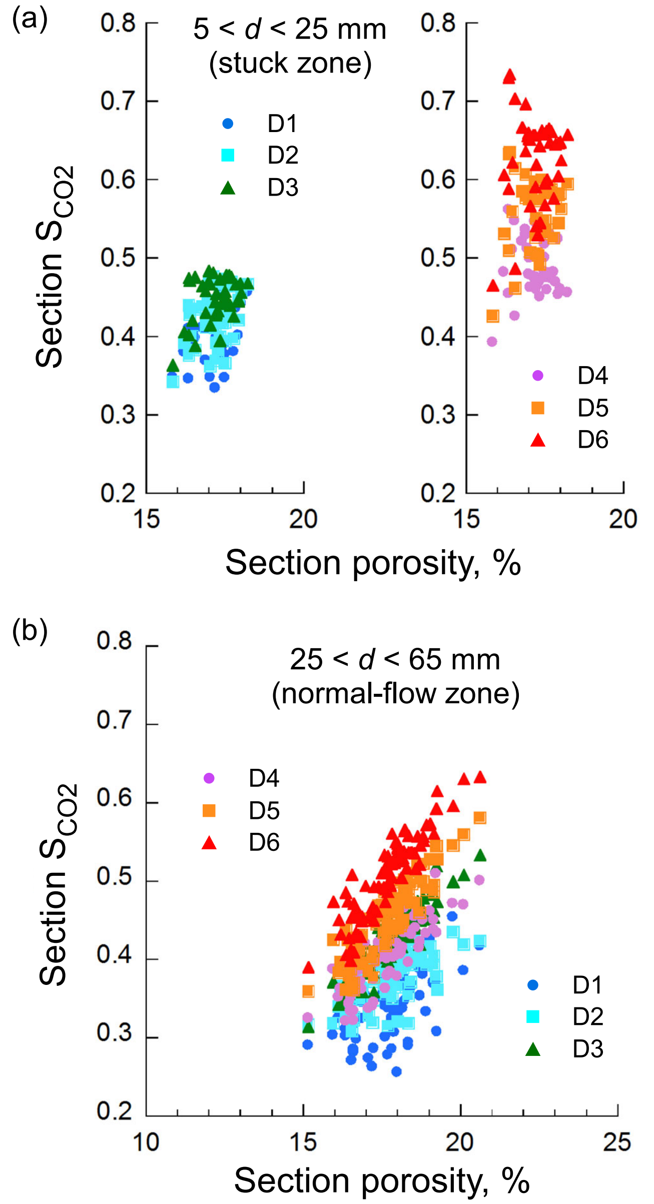

Figure 11. The relationship between the sectional S_{CO2} and the sectional averaged porosity within the areas (a) $5 < d < 25$ mm and (b) $25 < d < 65$ mm for all runs. (Colour in online-only publication).

5 RELATIVE PERMEABILITY CURVES AND FLOW REGIME

5.1 Relative permeability curves

Fig. 14 shows RPCs for brine and CO_2 of the present experiment, together with two other experiments for Berea sandstone by Perrin & Benson (2010) and Kogure *et al.* (2013). Flow directions of the cited experiments are parallel to the bedding layer. In this subsection, we describe features of our present results on RPCs with regard to rock heterogeneity and pathway formation.

In the present experiment, the high S_{CO2} region in the stuck zone became remarkable as CO_2 injection ratio was increased. Since a considerable amount of remnant CO_2 ganglia were left in the stuck zone and they were mostly isolated from the percolation pathways, the unique relationship between CO_2 saturation and capillary pressure will not be applicable in the stuck zone. We therefore

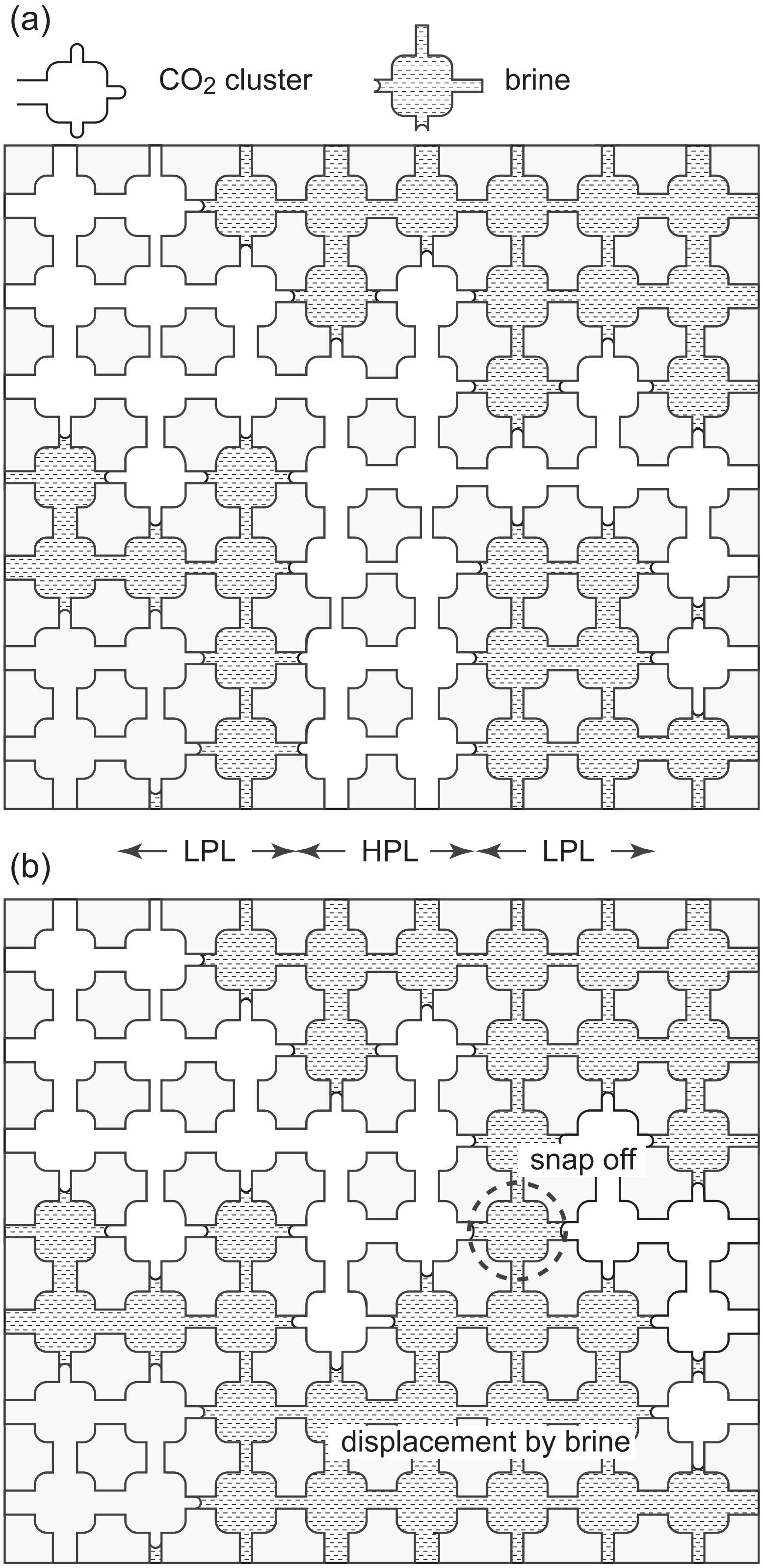

Figure 12. A 2-D conceptual model showing how ganglion dynamics affects the morphology of CO_2-filled percolated pathways. HPL and LPL are distinguished by differences in the ratio of wide to narrow pore throats. (a) CO_2- and brine-filling pore bodies and pore throats are shown by open and shaded, respectively. (b) Disconnection of the percolated CO_2 pathway by the brine snap off at the critical path due to a pressure drop in CO_2. The connected CO_2 pathway is also narrowed by the brine invasion through pores and pore throats. When the CO_2 pressure increases, brine is again pushed back. In HPL, CO_2 extends through wide pore throats because of lower capillary threshold pressures at wider pore throats.

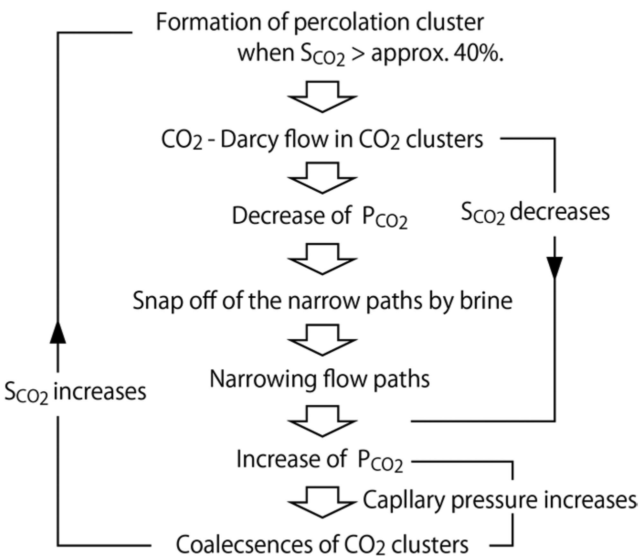

Figure 13. A sequence diagram for widening and narrowing of CO_2 percolation pathway. Decrease of the local P_{CO2} occur when local S_{CO2} exceeds about 40 per cent, which is the critical saturation for CO_2 percolation pathway. Brine snap-off events occur following the pressure decrease in the percolated CO_2 pathway. Local P_{CO2} increases again by continued flow of CO_2 which brings coalescences of CO_2 ganglia. Then percolated CO_2 pathway again appear, and CO_2 flows quickly through the percolated pathway causing another pressure drop inside the percolated pathway.

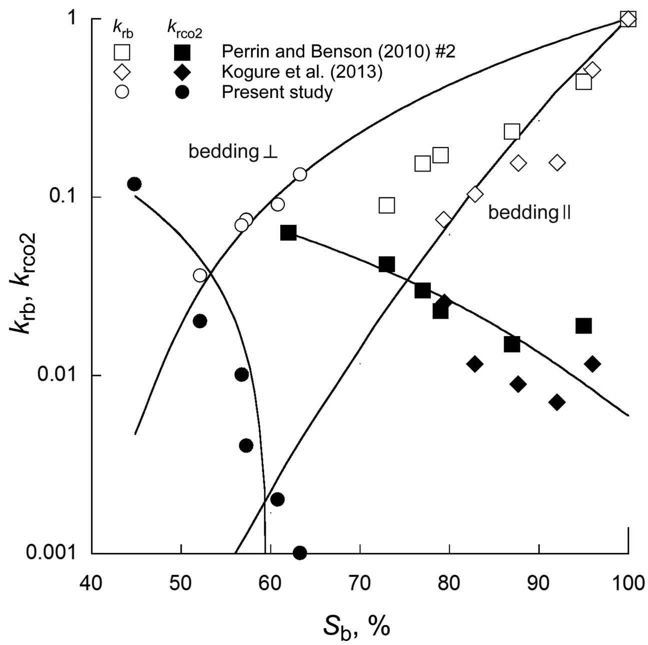

Figure 14. Relative permeability plots from this study (circle: bedding ⊥) together with the results of Perrin & Benson (2010) and Kogure *et al.* (2013) (bedding ||). Those experiments were performed with low flow velocities. Horizontal axis shows S_b, brine saturation, and vertical axis shows k_{rb} and k_{rCO2}, relative permeability of brine and CO_2, respectively.

eliminated the stuck zone for calculating the CO_2 saturation and used the average CO_2 saturation over the normal-flow zone $25 < d < 65$ mm for plotting RPC. Even if we use the average over the entire imaged zone, the S_{CO2} increases less than 3 per cent, except for run D6. Since values of ΔP in runs D1 and D2 are still increasing (Fig. 7), the relative permeability of CO_2 will be smaller than the values in Table 1. However, the differences will be very small and will not affect the RPC.

In all the experiments y described in the literature so far, and in contrast to our experiments, fluid injections were performed on core with bedding parallel to the core axis. In what follows, we use the terms ‘parallel core’ and ‘perpendicular core’ to refer to flow direction with respect to the bedding layers in rock.

Carbon dioxide spreads throughout HPL before formation of connected pathways in LPL, and preferably migrates through HPL in the parallel core because of lower capillary threshold pressures in wide-aperture pores and pore throats in HPL. Once a connected pathway is formed between inlet and outlet of the core, the pathway works as a channel where CO_2 can efficiently migrate. Steady-state flow is reached after formation of the channel which has enough flow capacity. In perpendicular core, no data appear until S_{CO2} becomes 34 per cent ($S_b = 66$ per cent), whereas, in the parallel core, data appear in the brine-rich side with S_{CO2} less than 10 per cent ($S_b = 90$ per cent). This suggests a threshold of CO_2 saturation for formation of a steady-flow channel in the perpendicular core.

5.2 Flow characteristic through channel and random pathways

Sectional images in perpendicular core and parallel core indicate two characteristic pathways: channeled pathway and randomly distributed pathway. Reynolds & Krevor (2015) used ‘parallel core’ having weak layered inhomogeneity, and conducted experiments of concurrent CO_2 and brine injection by controlling viscosity and density ratios between super critical CO_2 and brine under different pressure and temperature conditions. They revealed that channeled pathways or randomly distributed pathways distinctly appear depending on viscosity and density conditions of CO_2 and brine. Fig. 15 shows the relationship between S_b and pressure gradient of core at steady-flow states. Data are from Perrin & Benson (2010), Kogure *et al.* (2013), Reynolds & Krevor (2015) and this study. There are two types in the relationship, grouped as Types A and B. The cited experiments were made with different flow rates. The plotted relationships were clearly grouped into two different types regardless of flow rates; though pressure gradient generally depends on flow rate. The two types come out depending on pathway patterns. If random pathways are dominant in a core, the relationship belongs to the Type A. If channeled pathways are remarkable in a core, the relationship belongs to the Type B. Appearance of the types relates to inhomogeneity and flow direction as denoted as ‘parallel core’ or ‘perpendicular core’ when a core has layered inhomogeneity. However, the relationship between inhomogeneity and flow direction is not a unique factor that controls occurrence of the types. The data quoted from Reynolds & Krevor (2015) are all for parallel cores but the relationships belong to both Types A and B. The data from the first sample of Perrin & Benson (2010) are for the perpendicular core. Their image data on the axis-perpendicular sections showed distinct channeled pathways.

The data-missing region at the brine-rich area in Type A is due to the gap in CO_2 saturation until reaching a critical saturation value for forming CO_2 percolation cluster in core through movement and coalescence of CO_2 ganglia. The critical saturation value between 35 and 40 per cent for percolation clusters in randomly distributed pathways has been studied (e.g. Stauffer & Aharony 1994; Sahimi 1995). This implies that any kind of fluid forms percolated pathways in porous media when its saturation becomes 35–40 per cent. Percolated pathways for two types of fluid can coexist when the saturation value of each fluid exceeds 35–40 per cent. For this study,

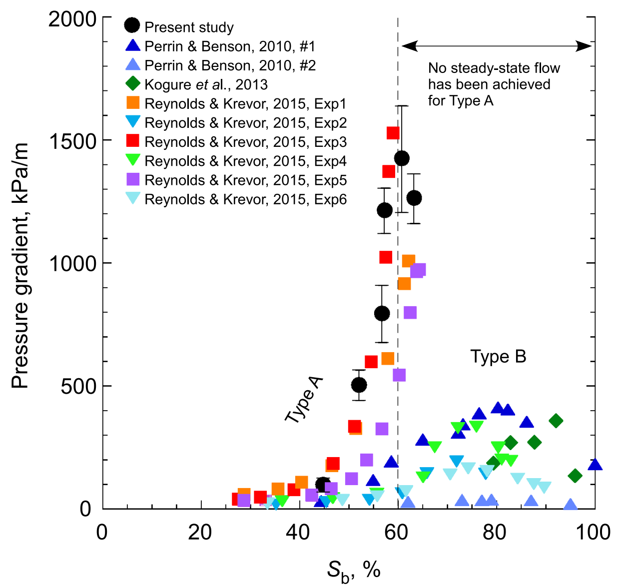

Figure 15. The relationship between S_b and pressure gradient obtained from this study and other studies. The pressure gradient is the differential pressure across a core divided by core length. Each bar shows the range of 1σ. There are two types in the relationship, grouped as Types A and B. The relationship belongs to the Type A if pathways are distributed randomly and to the Type B if channeled pathways are remarkable in a core. (Colour in online-only publication).

in addition to the pre-existing percolated pathways of brine, stable percolated pathways of CO_2 appears to have been fully developed in run D3 where the differential pressure started to decrease (Table 1 and Fig. 15). The critical value is also related to deviation from Archie's (1942) power law in the electrical resistivity index (Suman & Knight 1997; Han *et al*. 2009; Bauer *et al*. 2011; Li *et al*. 2015). In random pathways, the S_{CO2} values somewhere between 35 and 40 per cent are close to the pore-network saturation values corresponding to the inflection points of resistivity index in sandstones (Diederix 1982; Hunt & Idriss 2009). Therefore, it is reasonable to consider that the data gap in Type A is closely related to the formation of percolation cluster for the CO_2 pathway in sandstones.

In Type A, the rapid decrease of pressure gradient with the small increments of S_{CO2} from about 40 per cent to 50 per cent suggests growth of channel flow through percolated pathways. The small increments in S_{CO2} cause significant increase of percolated pathway capacity resulting in the sharp decrease of ΔP. This can be explained based on the classical percolation theory, if we assume that S_{CO2} represents probability of site or bond occupation in a random network. Percolation clusters grow drastically when the occupation probability becomes slightly over the percolation threshold (Hoshen *et al*. 1979).

6 CONCLUSIONS

Simultaneous injections of brine and CO_2 were performed in Berea sandstone. Injection was made perpendicular to the sediment-layer heterogeneity and with very low fluid flow velocity. An RPC of CO_2 and brine in Berea sandstone was also measured for the drainage process. The results show that differential pressure across the core decreases with increasing CO_2 content in the injected fluid at the end of each measurement run. This suggests the transition of the flow regime of CO_2 is from ganglion dynamics to connected-pathway flow, as revealed from μCT images (Armstrong *et al*. 2016). Fluid migration in larger scale, such as core scale, can therefore be successfully interpreted from micro-scale flow mechanisms (although further investigations are required to understand the mechanisms more precisely).

Bedding planes parallel to the flow direction allow creation of percolation clusters (channels) from the lower saturation value (0–10 per cent) for achievement of steady state**.** In contrast, perpendicular flow mostly creates randomly distributed pathways in each layer, resulting in a critical saturation (35–40 per cent) for achieving steady flow. The critical saturation value is close to those reported in electrical resistivity in sandstones where the resistivity deviates from Archie's law at a saturation smaller than 35–40 per cent.

The effect of bedding layers is also found in the shapes of RPCs. The brine-rich saturation endpoint of the RPC showed more CO_2 saturation (*ca*. 40 per cent), suggesting that high CO_2 saturation is necessary to form CO_2 percolation clusters that connect inlet and outlet sample ends.

ACKNOWLEDGEMENTS

We acknowledge R. Kranz for valuable comments and suggestions to this manuscript. Data to support this article are from the Ministry of Economy, Trade and Industry of Japan (METI) under the research contract 'Development of Safety Assessment Technology for Carbon Dioxide Capture and Storage,' and are available through contact with the corresponding author (TK, kogure@riko.shimane-u.ac.jp).

REFERENCES

Akbarabadi, M. & Piri, M., 2013. Relative permeability hysteresis and capillary trapping characteristics of supercritical CO_2/brine systems: an experimental study at reservoir conditions, *Adv. Water Resour.,* **52,** 190–206.
Akin, S. & Kovscek, A.R., 2003. Computed tomography in petroleum engineering research, *Geol. Soc. Lond. Spec. Pub.,* **215,** 23–38.
Alemu, B.L., Aker, E., Soldal, M., Johnsen, Ø. & Aagaard, P., 2013. Effect of sub-core scale heterogeneities on acoustic and electrical properties of a reservoir rock: a CO_2 flooding experiment of brine saturated sandstone in a computed tomography scanner, *Geophys. Prospect.* **61,** 235–250.
Al-Menhali, A.S., Menke, H.P., Blunt, M.J. & Krevor, S.C., 2016. Pore scale observations of trapped CO_2 in mixed-wet carbonate rock: applications to storage in oil fields, *Environ. Sci. Technol.,* **50,** 10282–10290.
Andrew, M., Bijeljic, B. & Blunt, M.J., 2013. Pore-scale imaging of geological carbon dioxide storage under in situ conditions, *Geophys. Res. Lett.,* **40,** 3915–3918.
Andrew, M., Menke, H., Blunt, M.J. & Bijeljic, B., 2015. The imaging of dynamic multiphase fluid flow using synchrotron-based x-ray microtomography at reservoir conditions, *Transp. Porous Media,* **110,** 1–24.
Archie, G.E., 1942. The electrical resistivity log as an aid in determining some reservoir characteristics, *Trans. Am. Inst. Min. Metall. Eng.,* **146,** 54–62.
Argaud, M., Giouse, H., Straley, C., Tomanic, J. & Winkler, K., 1989. Salinity and saturation effects on shaly sandstone conductivity, in *64th SPE Annual Technical Conference and Exhibition,* 8–11 October, San Antonio, Texas.
Armstrong, R.T., McClure, J.E., Berrill, M.A., Rücker, M., Schlüter, S. & Berg, S., 2016. Beyond Darcy's law: the role of phase topology and ganglion dynamics for two-fluid flow, *Phys. Rev. E,* **94,** doi:10.1103/PhysRevE.94.043113.
Azo materials, 2003a. Polyethylene terephthalate polyester (PET, PETP)—properties and applications—supplier data by good fellow. Available at: http://www.azom.com/article.aspx?ArticleID=2047, last accessed 16 August 2016.

Azo materials, 2003b. Polyvinylidenechloride (PVDC)—properties and applications—supplier data by good fellow. Available at: http://www.azom.com/article.aspx?ArticleID=2004, last accessed 16 August 2016.

Bauer, D., Youssef, S., Han, M., Bekri, S., Rosenberg, E., Fleury, M. & Vizika, O., 2011. From computed microtomography images to resistivity index calculations of heterogeneous carbonates using a dual-porosity pore-network approach: influence of percolation on the electrical transport properties, *Phys. Rev. E,* **84,** doi:10.1103/PhysRevE.84.011133.

Berg, S. *et al.*, 2013. Real-time 3D imaging of Haines jumps in porous media flow, *Proc. Natl. Acad. Sci. USA,* **110,** 3755–3759.

Berg, S. *et al.*, 2016. Connected pathway relative permeability from pore-scale imaging of imbibition, *Adv. Water Resour.,* **90,** 24–35.

Brooks, R.H. & Corey, A.T., 1964. Hydraulic properties of porous media, Hydrology Paper No. 3, Colorado State University, pp. 1–27.

Diederix, K.M., 1982. Anomalous relationships between resistivity index and water saturations in the Rotliegend sandstone (The Netherlands), in *SPWLA 23rd Annual Logging Symposium,* 16 pp., 6–9 July, Corpus Christi, Texas.

Han, M., Youssef, S., Rosenberg, E., Fleury, M. & Levitz, P., 2009. Deviation from Archie's law in partially saturated porous media: wetting film versus disconnectedness of the conducting phase, *Phys. Rev. E,* **79,** doi:10.1103/PhysRevE.79.031127.

Hoshen, J., Klymko, P. & Kopelman, R., 1979. Percolation and cluster distribution. III. Algorithms for the site-bond problem, *J. Stat. Phys.,* **21,** 583–600.

Hunt, A.G. & Idriss, B., 2009. Percolation-based effective conductivity calculations for bimodal distributions of local conductances, *Phil. Mag.,* **89,** 1989–2007.

Kogure, T., Nishizawa, O., Chiyonobu, S., Yazaki, Y., Shibatani, S. & Xue, Z., 2013. Effect of sub-core scale heterogeneity on relative permeability curves of porous sandstone in a water-supercritical CO_2 system, *Energy Procedia,* **37,** 4491–4498.

Krause, M.H. & Benson, S.M., 2015. Accurate determination of characteristic relative permeability curves, *Adv. Water Resour.,* **83,** 376–388.

Krevor, S.C.M., Pini, R., Zuo, L. & Benson, S.M., 2012. Relative permeability and trapping of CO_2 and water in sandstone rocks at reservoir conditions, *Water Resour. Res.,* **48,** doi:10.1029/2011WR010859.

Lenormand, R., Touboul, E. & Zarcone, C., 1988. Numerical models and experiments on immiscible displacements in porous media, *J. Fluid Mech.,* **189,** 165–187.

Li, M., Tang, Y., Bernabé, Y., Zhao, J., Li, X., Bai, X. & Zhang, L.H., 2015. Pore connectivity, electrical conductivity and partial water saturation: network simulations, *J. geophys. Res.,* **120**(6), 4055–4068.

Perrin, J.-C. & Benson, S., 2010. An experimental study on the influence of sub-core scale heterogeneities on CO_2 distribution in reservoir rocks, *Transp. Porous Media*, **82**(1), 93–109.

Pini, R. & Benson, S.M., 2013. Simultaneous determination of capillary pressure and relative permeability curves from core-flooding experiments with various fluid pairs, *Water Resour. Res.,* **49,** 3516–3530.

Reynolds, C.A. & Krevor, S., 2015. Characterizing flow behavior for gas injection: relative permeability of CO_2-brine and N_2-water in heterogeneous rocks, *Water Resour. Res.,* **51,** 9464–9489.

Rücker, M. *et al.*, 2015. From connected pathway flow to ganglion dynamics, *Geophys. Res. Lett.,* **42,** 3888–3894.

Ruprecht, C., Pini, R., Falta, R., Benson, S. & Murdoch, L., 2014. Hysteretic trapping and relative permeability of CO_2 in sandstone at reservoir conditions, *Int. J. Greenhouse Gas Control,* **27,** 15–27.

Sahimi, M., 1995. *Flow and Transport in Porous Media and Fractured Rock,* VCH, p. 482.

Span, R. & Wagner, W., 1996. A new equation of state for carbon dioxide covering the fluid region from the triple-point temperature to 1100 K at pressures up to 800 MPa, *J. Phys. Chem. Ref. Data,* **25,** 1509–1596.

Stauffer, D. & Aharony, A., 1994. *Introduction to Percolation Theory,* revised 2nd edn., Taylor & Francis, p. 192.

Suman, R.J. & Knight, R.J., 1997. Effects of pore structure and wettability on the electrical resistivity of partially saturated rocks—a network study, *Geophysics,* **62,** 1151–1162.

Tallakstad, K.T., Løvoll, G., Knudsen, H.A. & Ramstad, T., 2009. Steady-state simultaneous two-phase flow in porous media: an experimental study, *Phys. Rev. E,* **80,** doi:10.1103/PhysRevE.80.036308.

Valavanides, M.S., Constantinides, G.N. & Payatakes, A.C., 1998. Mechanistic model of steady-state two-phase flow in porous media based on ganglion dynamics, *Transp. Porous Media,* **30,** 267–299.

Zhang, Y., Nishizawa, O., Kiyama, T., Chiyonobu, S. & Xue, Z., 2014. Flow behaviour of supercritical CO_2 and brine in Berea sandstone during drainage and imbibition revealed by medical X-ray CT images, *Geophys. J. Int.,* **197,** 1789–1807.

Zhang, Y., Nishizawa, O., Kiyama, T. & Xue, Z., 2015. Saturation-path dependency of P-wave velocity and attenuation in sandstone saturated with CO_2 and brine revealed by simultaneous measurements of waveforms and X-ray computed tomography images, *Geophysics,* **80,** D403–D415.